Realistic turbulent inflow conditions for estimating the performances of a floating wind turbine

Cédric Raibaudo[1,2], Jean-Christophe Gilloteaux[1], and Laurent Perret[1]

[1]Nantes Université, Centrale Nantes, CNRS, LHEEA, UMR 6598, F-44321 Nantes, France
[2]University of Orléans, INSA-CVL, PRISME, EA 4229, 45072, Orléans, France

Correspondence: Laurent Perret (laurent.perret@ec-nantes.fr)

Abstract. A novel method for generating turbulent inflow boundary conditions for aeroelastic computations is proposed, based on interfacing hybrid hot-wire and particle image velocimetry measurements performed in a wind tunnel to a full-scale load simulation conducted with FAST. This approach is based on the use of the proper orthogonal decomposition (POD) to interpolate and extrapolate the experimental data onto the numerical grid. The temporal dynamics of the temporal POD coefficients is driven by the high-frequency hot-wire measurements used as inputs of lower-order model built using a multi time-delay linear stochastic estimation (LSE) approach. Being directly extracted from the data, the generated 3-component velocity fields later used as inlet conditions present correct one- and two-point spatial statistics and realistic temporal dynamics. Wind tunnel measurements are performed at a scale of 1:750, using a properly scaled porous disc as a wind turbine model. The POD analysis of the flow, with or without taking into account the presence of the surge motion of the model, shows that a few modes are able to capture the characteristics of the most energetic flow structures and the main features of the wind turbine wake such as its meandering and the influence of the surge motion. The interfacing method is first tested to estimate the performance of a wind turbine in an offshore boundary layer and then those of a wind turbine immersed in the wake of an upstream wind turbine subjected to a sinusoidal surge motion. Results are also compared to those obtained using the standard inflow generation method provided by TurbSim available in FAST.

1 Introduction

For the recent years, floating offshore wind turbines (FOWT) have been of particular importance for both scientific and industrial applications. Mounted on a floating structure, these turbines can be installed in deep waters, with wider space and more available power, compared to onshore and fixed offshore wind turbines. Understanding wind turbines' wakes is crucial to improve their aerodynamics when operating in farms (Schmidt and Stoevesandt, 2015; Bastine et al., 2018). For FOWT embedded in farms, multi-dynamics and multi-scale phenomena can impact the wake characteristics and therefore the farm performances (Huang et al., 2018). In particular, the wake interaction between FOWTs significantly affects the power produced by the farms and needs to be considered carefully (Huang et al., 2018).

For the modelling and the prediction of the wind turbine wake, simplified analytic models have been suggested based mostly on the mean velocity deficit (Jensen, 1983; Frandsen et al., 2006; Bastankhah and Porté-Agel, 2014). These models could lack

of precision but are easier to compute, compared to high-cost simulations, especially for wind farms control. Other parameters such as the turbulence intensity, the geometrical properties (turbine diameter D, position in the wake x/D, roughness length z_0, etc.), the thrust, can be included in the models for better representativity (review of Kaldellis et al. (2021) for more details).

As for experimental works, as multiple blades rotors are usually difficult to use due to the scaling and similitude with the incoming flow, porous discs have been employed in the past to model wind turbines. This approach is similar to the actuator disc theory used for theoretical and numerical prediction of wind turbine performances, in which the rotor is replaced by a permeable disc generating an equivalent thrust (Betz, 1920; Joukowsky, 1920). Pioneer study of Aubrun et al. (2013) showed that the mean velocity deficit, the integral scales and the statistics of the porous disc wake are similar to those of a model with rotor for downstream positions in the wake $x/D > 3$. Similar conclusions were found by Camp and Cal (2016) for $x/D > 3.5$. Porous discs are therefore valid for the characterization of the far-field wake, where, in farms, other downstream wind turbines are expected to be located.

Unsteady phenomena occur in the wind turbine wake, and in particular the wake meandering. Even if the associated physical mechanism is still not fully understood today, meandering is a large-scale motion of the wake due to the interaction between the rotor and large coherent structures of the incoming boundary layer (Porté-Agel et al., 2020; Hodgkin et al., 2023). The meandering is also sensitive to the incoming flow conditions, such as the turbulence level (Foti et al., 2018; Porté-Agel et al., 2020).

For FOWTs, the unsteady behavior of the wake interacts with the wave-induced motion of the platform. Rockel et al. (2014) firstly studied the effect of one of the motion component - the pitch - on the wake dynamics with stereoscopic Particle Image Velocimetry (PIV). The study showed that the motion creates additional vertical velocity and reduces the kinetic energy available for a downwind turbine. Khosravi et al. (2015) considered the surge motion and also observed a slow-down of the wake recovery and a decrease of the kinetic energy, but an increase of 1 % of power produced for the given turbine. By considering pitch and roll experimentally, Fu et al. (2019) showed no effect of the motions on the mean power produced. However, the pitch motion reduces the power fluctuations in the lowest frequency part of the spectrum, for frequencies lower than the imposed pitch motion harmonics. The roll motion also reduces these fluctuations around a specified frequency, about the half of the motion main harmonics. On the other hand, Corniglion et al. (2020) observed the effect of a high-frequency surge motion, in particular an increase of the mean thrust and the axial velocity in the wake. Recent works (Messmer et al., 2022; Fontanella et al., 2022) investigated the effect of more complex motions on the wake dynamics and the meandering in particular. However these effects are still not fully understood for floating wind turbines. These difficulties of understanding increase when considering realistic atmospheric conditions for numerical and experimental studies. By varying the turbulence intensity of the incoming flow, significant differences in the wake properties and/or the power produced by the wind turbine can be observed (Saranyasoontorn and Manuel, 2005; Chamorro and Porté-Agel, 2009; Nybø et al., 2020). Other studies (Chamorro and Porté-Agel, 2009; Bastine et al., 2014; Schliffke, 2022) considered significant atmospheric turbulent boundary layer upstream the wind turbine. Axisymmetry of the incoming flow in particular plays an important role on the redistribution of the turbulence levels in the turbine wake (Chamorro and Porté-Agel, 2009).

As explained in the two previous paragraphs, taking into account realistic conditions of the incoming flow and wave-induced motions is crucial to estimate the performances of floating wind turbines. It is also clear today that atmospheric turbulence cannot be treated as a purely random phenomenon characterized only by its intensity. To address this problem, the strategy commonly used in the wind energy community is based on the generation of synthetic turbulence with a target spectral content representative of the atmosphere (Kelley and Jonkman, 2007; Mann, 1998). This approach, implemented in the TurbSim turbulence generator of the FAST aeroelastic code of the National Renewable Energy Laboratory (NREL), has been improved to take into account particular phenomena such as low-level jets or Kelvin-Helmholtz instabilities that can develop in the atmosphere under certain conditions (Kelley and Jonkman, 2007). In the case of wind farm studies, the turbines are located in the wake of other machines; the synthetic turbulence approach can no longer be used directly and must be modified to take into account the presence of the wake so as to perform aeroelastic calculations under realistic realistic conditions. The developed approaches range from simple wake models imposing an additional velocity deficit to stochastic wake models based on LES (Large Eddy Simulation) type precursor computations through intermediate models taking into account the velocity deficit but also the meandering of the wake (see Bastine et al. (2018), and references herein).

In the context of LES computation of turbulent flows, Perret et al. (2006, 2008) proposed an alternative method to generate realistic unsteady inflow conditions by coupling wind tunnel measurements to an LES code to simulate a turbulent mixing layer flow. In their approach, non-time resolved stereoscopic PIV measurements were performed in a cross-section of the flow corresponding to the inlet section of the targeted LES simulation. Using Proper Orthogonal Decomposition (POD) to decompose the velocity fields into a set of spatial modes and temporal coefficients, a low-order representation of the flow was built. The time evolution of the temporal coefficients was modeled either in a purely stochastic manner via random Gaussian numbers with a realistic spectrum (Perret et al., 2006) or by deriving a low-order dynamical model of the temporal evolution of the most energetic structures (Perret et al., 2008). The incoherent motion was modeled by employing time series of Gaussian random numbers to mimic the temporal evolution of higher order POD modes. Beyond the fact that this innovative method allows for the study of complex flow configurations (as long as wind tunnel measurement can be performed), it enables the generation of inlet conditions with a realistic spatio-temporal organization, a feature often missing in purely stochastic approaches.

The present study aims to include the two above mentioned requirements to properly estimate FOWT performance: the generation of a wave-induced surge motion for the FOWT model, and realistic conditions with properly scaled boundary layer and turbulence level for the incoming flow. Building upon the work of Perret et al. (2006, 2008), a novel approach is proposed, by developing a direct coupling between experimental data from a scaled-down wind tunnel experiment and a full-scale load computational code (FAST from NREL in the present case). As detailed in the following, it relies on stereoscopic PIV performed in a cross-section of the wind-turbine wake combined with the derivation of a data-driven low order model to improve the temporal dynamics of the PIV measurements. This database of well time-resolved vector fields generated in the cross-section of the flow are then used as unsteady inlet conditions for the load computation. After a description of the experimental setup (§2), the mean wake will be presented (§3). Scaling details between the model and a real scale prototype will be discussed (§4). The velocity fields needs to be reconstructed at high-sampling frequency using stochastic estimation

(§5), before being coupled to FAST simulations to evaluate the power produced by a downwind floating wind turbine submitted to the wake under surge motion (§6).

95   2   Experimental setup

(a)   (b)
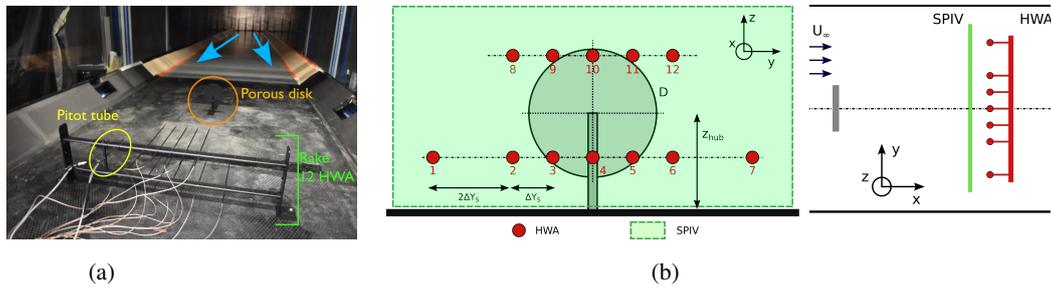
Figure 1. Experimental setup: (a) picture of the setup in the wind-tunnel and (b) schemes of the metrology setup.

Experiments were carried in the LHEEA lab's atmospheric wind tunnel. The experimental setup is presented in Fig. 1. The wind turbine is modeled using a porous disk of diameter $D = 0.16$ m. The disk center is set at a height $z_{hub} = 0.12$ m with respect to the floor. The model represents the floating 2MW wind turbine used in the FLOATGEN research project, installed at Centrale Nantes' offshore test site in Le Croisic, France (Rousset et al., 2010). The thrust coefficient C_t is estimated to be

100   approximately 0.5 and the power coefficient $C_p \approx 0.25$ (Schliffke et al., 2020). For streamwise positions x/D in the wake further than 3, the use of porous disks for the characterization of wind turbines wakes is considered valid (Schliffke et al., 2020). Without model, the free-stream velocity is $U_\infty = 4.2$ m/s and the turbulent intensity about 0.5%. The thickness of the incoming boundary layer is $\delta = 0.6$ m and the resulting Reynolds number is $Re = U_\infty \delta / \nu \approx 160\,000$.
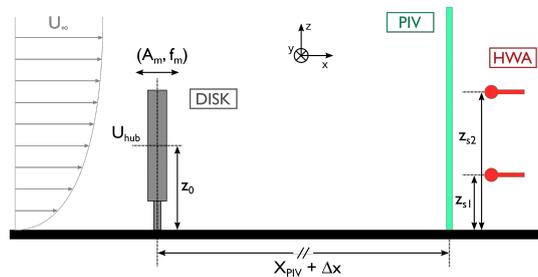
Figure 2. Sketch of the wave-induced surge motion experimental setup.

To replicate realistic behaviors of floating wind turbines under wave swell, a sinusoidal surge-motion is imposed on the

105   model using a linear actuator (Schliffke et al., 2020). The setup to model this motion is presented in Fig. 2. The sinusoidal amplitude is ± 0.01 m and the frequencies tested $f_m = [0, 2, 3, 3.75]$ Hz. Using the incoming velocity speed and the disk diameter, it corresponds to a non-dimensionalized frequency $F_m^+ = f_m \, D \, / \, U_\infty = [0, 0.08, 0.11, 0.14]$. The model position

is controlled retroactively and monitored, with a bias of about 1 mm between the expected and real positions (Schliffke et al., 2020). As indicated in Fig. 2, the variable x-axis corresponds to the flow direction, the $y - z$ plane is normal to the flow. The coordinates origin is chosen at the disk center.

Instantaneous three-components velocities of the wake were acquired using stereoscopic PIV in a $y - z$ plane normal to the main flow direction, at two streamwise positions $x/D = 4.6$ and 8.1 downstream of the wind turbine model. Two $2560 \times 2160px^2$ sCMOS Zyla cameras from Oxford Instruments were set upstream on each side of the wind tunnel. Nikon lens with a focal of $f_o = 60$ mm were fixed on the cameras. Scheimpflug adapters were used to ensure a focused image over the full field of view. The laser sheet was generated using a double pulse Nd-Yag laser (200 mJ per cavity). A LaVision Laskin-Nozzle aerosol generator was used to seed with olive oil droplets of 1 μm diameter. Transparent film was added at the walls to reduce the light diffusion. The time delay between the two pulses was $dt_{PIV} = 300$ μs. Image analysis was performed using a standard cross-correlation multi-pass algorthim with a final interrogation window size of 32×32 px^2 using Dantec Dynamics software. The size of the final region of interest is about $3D \times 2D$. The sampling frequency is $f_{PIV} = 14.1$ Hz and 14000 snapshots were acquired for each case. The number of snapshots was doubled for one case to estimate the statistical convergence.

Constant temperature anemometry (CTA) measurements were also performed simultaneously to the PIV. Twelve hot-wire (HWA) sensors were distributed spanwise, downstream the PIV measurement plane and at two heights ($0.47D$ and $1.25D$). The sampling frequency for the sensors was $f_{HWA} = 15$ kHz. Sensors were calibrated using King's law by measuring the free-stream flow with the help of a Pitot tube. The calibration procedure and the post-processing of the raw voltages accounted for temperature correction using the method proposed by Hultmark and Smits (2010).

3   Mean structure of the flow

The mean wake flow is documented with the present experimental campaign. Streamwise mean and RMS velocity fields are presented in Fig. 3. Two streamwise positions in the wake are presented here: $x/D = 4.6$ and 8.1. The mean flow in the near-wake is disturbed by the disk, following its shape (represented with dash line in Fig. 3). At $x/D = 8.1$, the wake center is slightly shifted to the negative y-direction, also seen in previous works (Schliffke et al., 2020; Foti et al., 2019). It could correspond to the small spanwise velocity of the incoming flow observed previously (Raibaudo and Perret, 2022). Compared to the flow without model, the turbulence intensity increases in the near-wake from 8 % up to 15 %. The circular horseshoe shape in the near-wake has been found in previous works (Hamilton et al., 2018). The slight shift in the negative y-direction is observed in the RMS fields at $x/D = 8.1$. More details on the mean flow can be found in Schliffke et al. (2020) and Belvasi et al. (2022).
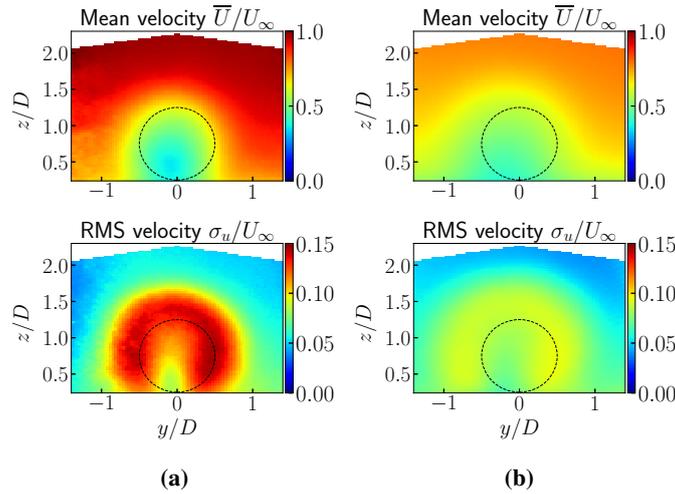
Figure 3. Streamwise mean $\overline{U}/U_\infty$ (first row) and RMS velocity σ_u/U_∞ (second row) for: (a) wake for the fixed model at $x/D = 4.6$ and (b) wake for the fixed model at $x/D = 8.1$. Dashed lines correspond to the position of the porous disk in the $Y - Z$ plane.

4 Scaling

The experimental setup presented in the previous section has been chosen to respect scaling properties between the model and the chosen prototypes. A complete study on how to scale wind turbines rotors has been developed by Canet et al. (2021) for example, and a full explanation of the scaling methodology for the present case can be found in Schliffke (2022). As the

140 numerical model of the FLOATGEN prototype or its detailed characteristics are not available for the FAST simulations due to confidentiality constraints, the 5MW reference wind turbine is used (Jonkman et al., 2009). The full-scale rotor diameter is $D_P = 120$ m, the hub height $z_{0,P} = 90$ m, the atmospheric boundary layer about $\delta \approx 300$ m and the incoming velocity at the hub height $U_{0,P} = 10$ m/s, also corresponding to the parameter implemented in the present FAST simulations.

Therefore, scaling factors are determined between the model and the NREL reference wind turbine. First, the geometric

145 scaling factor based on the rotor diameter is $\Lambda_L = D_P/D = 750$. The porous disk diameter is chosen to respect a blocking factor of 0.5 %, which is under the 5 % required by the VDI guideline 3783 (VDI, 2017). The model hub height is fixed at $z_0 = 0.12$ m to be totally immersed in the boundary layer of height $\delta = 0.6$ m. It corresponds to the NREL hub height of 90 m immersed in atmospheric boundary layers of values between 300 and 500 m.

The velocity scaling factor is defined using the hub velocity by $\Lambda_V = U_{hub,P}/U_{hub}$. The standard objective for FAST

150 simulations is $U_{hub,P} = 10$ m/s. For the model, for a freestream velocity of $U_\infty = 4.2$ m/s, the velocity at hub height in the undisturbed oncoming boundary layer is $U_{hub} = 3.8$ m/s. The scaling factor is therefore $\Lambda_V = 2.6$. Using Strouhal number similarity, the time scaling factor is $\Lambda_t = \frac{\Lambda_L}{\Lambda_V} = 284$. This means physical phenomena in the wind tunnel occurs 284 faster than for the prototype. For the FAST implementation with this time factor, to simulate the aerodynamics at a classical sampling

frequency around 20 Hz, velocity fields are therefore needed at a minimal frequency of 5680 Hz. Reconstruction of the velocity
fields at a frequency higher than that of the PIV measurements is therefore necessary.

As detailed by Schliffke (2022), the imposed surge-motion frequency is chosen based on measurements made for the FLOAT-
GEN prototype. The sea state taken as reference for this floating wind turbine is of height $H_S = 4.6$ m and $T_P = 11$ s. With
the time scaling factor calculated previously, it leads to a wave-induced frequency about 25 Hz for the wind tunnel model. The
chosen actuator does not reach this value, but is of the same order of magnitude.

5   Stochastic reconstruction using POD-LSE multi-delays

For the coupling of wind-tunnel PIV velocity fields with an aeroelastic code to perform a full-scale load simulation, due to
the scaling constraints presented in §4, high-sampling frequency is required. By combining the velocity fields acquired with
PIV and time-resolved HWA measurements, stochastic approaches are used here to reconstruct velocity fields at high temporal
resolution.

5.1   Methodology

Reconstruction of the velocity fields is performed using a Proper Orthogonal Decomposition and multi-time-delay Linear
Stochastic Estimation (POD-mLSE) approach (Durgesh and Naughton, 2010), which is an extension of the standard POD-LSE
technique developed by Bonnet et al. (1994). Velocity fields are first decomposed into temporal and spatial modes using the
standard snapshot POD (Sirovich, 1987):

$$\mathbf{u}(\mathbf{x},t) \approx \sum_{i=0}^{N_m} a_i(t)\, \Phi_i(\mathbf{x}) \tag{1}$$

with N_m the number of modes selected for the truncature. Here, $N_m = 100$ modes are chosen, corresponding to about 80%
of the cumulative eigenvalues energy. The objective is to determine the more suitable coefficients B_{ijk} to express the relation
between the temporal modes a_i and the HWA sensors with time delays τ_k. The reconstructed temporal modes $\widehat{a}_i$ are then
estimated at higher sampling rate:

$$\widehat{a}_i(t) = \sum_{j=0}^{N_j} \sum_{k=0}^{N_k} B_{ijk}\, S_j(t - \tau_k) \tag{2}$$

with $N_j = 12$ the number of HWA sensors S_j and N_k the number of delays imposed on the sensors. Here, $N_k = 21$ de-
lays are distributed between ± 0.2 s, following comparable reconstruction parameters on similar experiments (Blackman and
Perret, 2016). The coefficients B_{ijk} are determined through the resolution of a least-square minimization problem using cross-
correlations:

$$B_{ijk} = \mathcal{C}_{\{a_i,\, S_{jk}\}}^{-1}\, \mathcal{C}_{\{S_{jk}\}} \tag{3}$$

with $\mathcal{C}_{\{a_i,\, S_{jk}\}}$ the cross-correlations between the temporal modes and the sensors with delays, and $\mathcal{C}_{\{S_{jk}\}}$ the correlations
between the different sensors with different delays. Temporal modes $\widehat{a}_i$ are therefore estimated at higher temporal resolution

using Eq. 2, then combined with the spatial modes using POD (Eq. 1) to reconstruct the velocities. Only results for the downstream location $x/D = 8.1$ are presented here, which corresponds to the inlet section of the load simulations. The sampling

185 frequency used for the reconstruction is $f_s = 7.05$ kHz, to meet the conditions required for these simulations.

5.2 Proper Orthogonal Decomposition

A selected set of results on the POD analysis is presented here. More details can be found in appendix A and in previous works from the authors (Raibaudo et al., 2022).
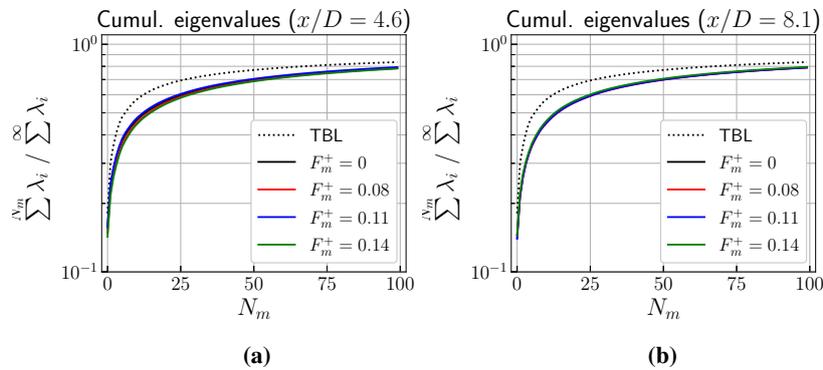
Figure 4. Cumulative eigenvalues $\sum\limits^{N_m} \lambda_i / \sum\limits^{\infty} \lambda_i$ from the POD obtained from different streamwise positions (a) $x/D = 4.6$ and (b) $x/D = 8.1$. For each configuration, four frequencies of motion F_m^+ are presented in solid lines: 0 (fixed), 0.08, 0.11 and 0.14. TBL without model is presented in dotted line.

The convergence using the cumulative eigenvalues $\sum\limits^{N_m} \lambda_i / \sum\limits^{\infty} \lambda_i$ is first shown in Fig. 4. The two streamwise positions in

190 the wake are considered, and compared with the POD modes for the turbulent boundary layer without model. Compared with typical bluff-body flows, the eigenvalues convergence is slow, due to the high Reynolds number incoming turbulent boundary layer. The eigenvalues are therefore comparable with previous works, in particular De Cillis et al. (2021): for a near-wake flow downstream a nacelle and tower model, the cumulative eigenvalues reached about 40 % after $N_m = 15$ modes, as it is about 50 % for the present study for the same number of modes.

195 Details on the spatial modes are presented in appendix A. It corresponds to the analysis performed in Raibaudo et al. (2022), and two salient features can be observed from it: (i) the structure of the spatial modes forming around the disk shape are similar to previous works on POD analysis on wind turbines wakes (Bastine et al., 2015), and (ii) no significant effect of the surge-motion can be found in the spatial modes. Modes profiles are close in amplitude and shape, shown here for the streamwise velocity modes, but also for the other velocities components v and w.

200 However, significant differences can be observed on the temporal modes. Premultiplied PSD of the temporal modes a_i are presented in Fig. 5 for the turbulent boundary layer without model and the two streamwise positions in the wake. Despite the low-sampling rate of the PIV system, the surge-motion imprint can be clearly identified.
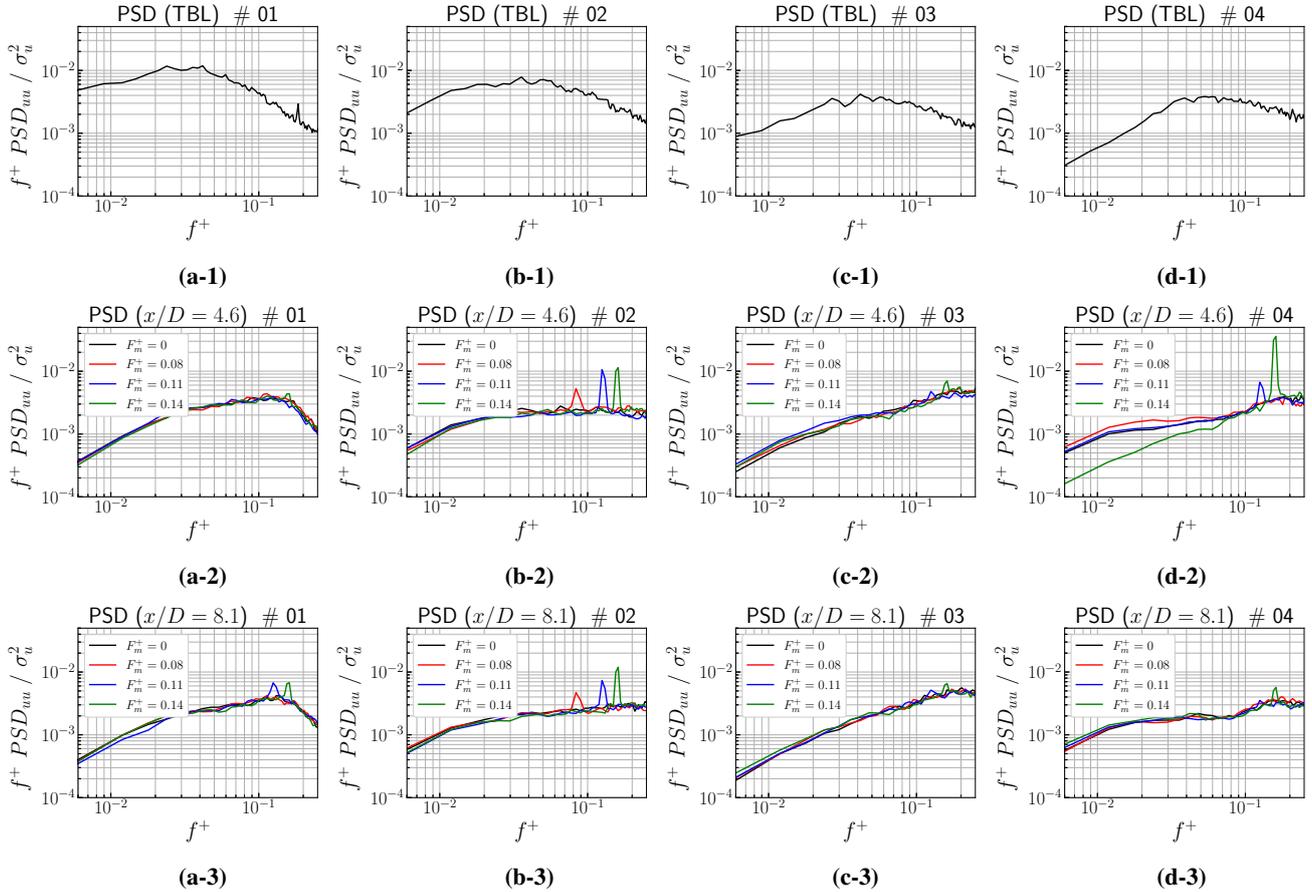
Figure 5. Premultiplied PSD of the temporal modes a_i obtained from different configurations: (1) TBL without porous disc, (2) wake at $x/D = 4.6$ and (3) wake at $x/D = 8.1$; (a-d) modes 1 to 4.

A broad spectrum is found for the flow without model, centered around the main reduced frequency at $f^+ = 0.04$ ($f \approx 1$ Hz). By considering the fixed porous disk wake, the spectra amplitude changes significantly and the main frequency is shifted

205 to $f^+ = 0.13$ ($f \approx 3$ Hz). The surge-motion is found to influence the temporal dynamics of the wake. In particular, the higher surge-motion frequencies have a greater influence on the wake: a motion at frequency $F_m^+ = 0.08$ shows similar dynamical behavior than the fixed model, where motions of $F_m^+ = 0.11$ and 0.14 shows the emergence of substantial peaks.

5.3 Physical interpretation of the modes dynamics

The relationship between the POD modes and the known physical phenomenon in wind turbine wakes is investigated by

210 considering the dynamics of the location of the wake center. The methodology corresponds to the one used by Bastine et al. (2015) and is used to estimate the center of the wake deficit. Using the deficit velocity $\tilde{\mathbf{u}}(\mathbf{x}, t) = U_0 - \mathbf{u}(\mathbf{x}, t)$, with U_0 the local freestream velocity, the center coordinates are calculated as:
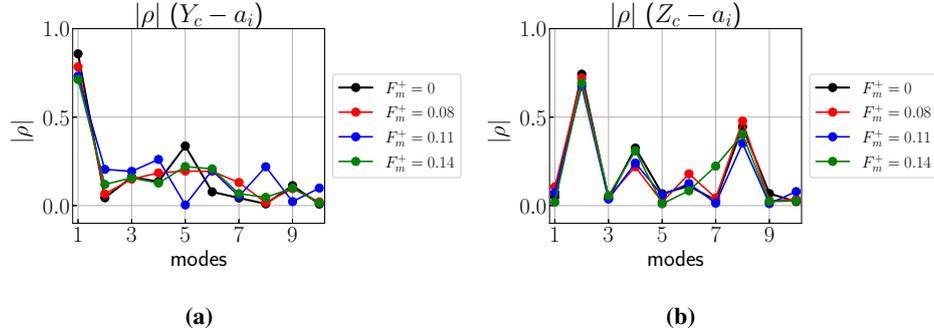
Figure 6. Absolute value of the Pearson's correlation coefficients between the (a) spanwise and (b) wall-normal coordinates and the temporal POD modes.

$$
\begin{bmatrix} y_c(t) \\ z_c(t) \end{bmatrix} = \frac{\iint \tilde{\mathbf{u}}^2(y,z,t) \begin{bmatrix} y \\ z \end{bmatrix} dy \, dz}{\iint \tilde{\mathbf{u}}^2(y,z,t) \, dy \, dz} \tag{4}
$$

Correlations of these coordinates with the POD temporal modes are presented in Fig. 6. Pearson's correlation coefficient is
215 considered here for the wake at $x/D = 8.1$. Conclusions are similar to the ones found by Bastine et al. (2015). The first mode strongly correlates with the spanwise motion of the wake, suggesting this mode corresponds to the horizontal meandering. The correlation decreases monotonically when the surge-motion frequency increases, from $\rho(y_c, a_1) = 0.86$ for the fixed model to 0.71 for $F_m^+ = 0.14$. This decrease of the correlation with mode 1 is counterbalanced on the next three modes. The second mode correlates instead better with the wall-normal wake motion, which could correspond to the downwash flow motion. The
220 correlation coefficient also decreases, from $\rho(z_c, a_2) = 0.74$ to 0.68 for $F_m^+ = 0.11$. Contrary to y_c, correlation between the wall-normal position z_c and the modes is maximum for modes 4 and 8.

5.4 Reconstruction using multi-time delay LSE

RMS profiles of the reconstructed along z are shown in Fig. 7. These statistics are compared with those of the original velocities obtained by the POD truncature (Eq. 1) with the same amount of modes $N_m = 100$ used in the reconstruction approach by the
225 stochastic methodology.

For the turbulent boundary layer (Fig. 7(a)), the streamwise RMS velocity profile σ_u/U_∞ is well reconstructed and reaches 60 %. The other reconstructed components σ_v and σ_w are underestimated (around 40 % for the spanwise and 50 % for the wall-normal component), but are still significant in amplitude. Same analysis can be made for the reconstruction of the wake flow (Fig. 7(b)). RMS of the reconstructed velocities are underestimated but show similar spatial distribution. Even if the stochastic
230 estimation looses information similarly to the TBL, this underestimation could be linked to the conditioning of the correlation
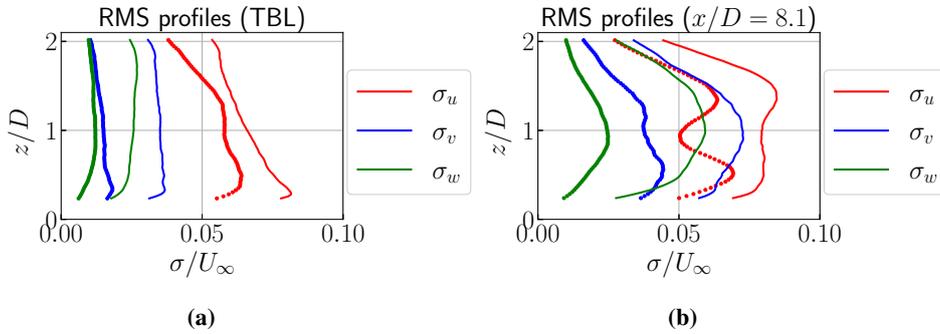
Figure 7. RMS reconstructed velocity u/U_∞ profiles along z using mtd-POD-LSE and original velocity using the same amount of modes $N_m = 100$. (a) TBL and (b) fixed model at $x/D = 8.1$. dots: truncated original PIV data, lines: mtd-POD-LSE data

matrix during the POD process. The inversion of this matrix could amplify the smaller eigenvalues for ill conditioned LSE problems (Podvin et al., 2018). However, the difference between the projected and the reconstructed velocities are comparable to previous works using the same approach (Dekou et al., 2015; Podvin et al., 2018). Furthermore, the presence of the model generates a three-dimensional wake which is well captured by the PIV but not well enough by the one-dimensional hot-wires,
235   which could also leads to errors.

Only the turbulent boundary layer and the far-wake for the fixed model were shown here, but the stochastic estimation was performed for the full database. By considering surge-motion, as its impact on the mean quantities is limited, the reconstructed profiles are similar than the ones presented in Fig. 7(b). For all the cases, the reconstructed velocities are reduced in amplitude by the POD-LSE process but conserves their main properties.
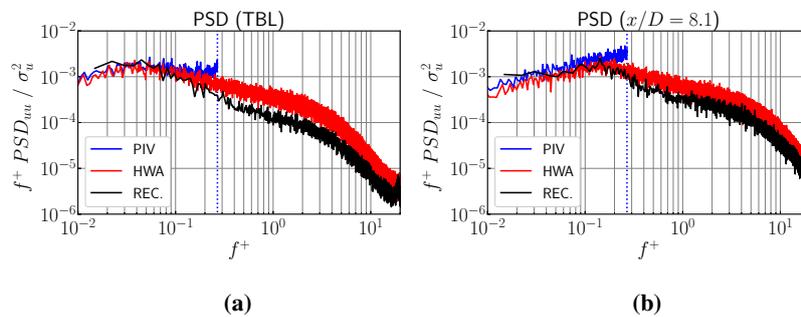
Figure 8. Premultiplied PSD of the reconstructed velocities at the hub height, compared to that directly measured by PIV or HWA. (a) TBL and (b) fixed model at $x/D = 8.1$. The vertical dashed line corresponds to the PIV sampling frequency limit.

240   Spectral analysis of the reconstructed streamwise velocity is presented in Fig. 8. Premultiplied PSD of the reconstructed velocity are compared with the ones estimated from the original PIV velocity truncated with the same amount of POD modes, and with a hot-wire sensor located at $y/D = 0$ and $z/D = 1.25$ (No. 10 on Fig. 1). The spectrum of the reconstructed velocity is consistent at low frequency with the PIV and follows well the dynamics behavior of the HWA sensor. A loss of spectrum

amplitude is also observed between the two, suggesting a loss of information at higher frequency with the stochastic recon-
struction as explained previously. Compared to the reconstructed turbulent boundary layer (Fig. 8(a)), the reconstructed wake
shows peaks at low frequency around $f^+ = \mathcal{O}(10^{-1})$, which is consistent as expected with the spectral analysis performed on
the temporal modes (Fig. 5).

6 Implementation for FAST simulations

Reconstructed velocity fields in the far field ($x/D = 8.1$) are now implemented as inflow wind conditions in FAST simulations,
where the effect of the surge-motion and the flow dynamics on the computed produced power are considered in the present
study.

6.1 Methodology

Spatial processing of the PIV velocity fields is first needed to adapt the velocity fields to the FAST requirements. As the
inflow wind conditions for FAST have to reach down the floor, the spatial POD modes are first extrapolated to be equal to
zero at the wall. Velocity fields are then reconstructed with these extrapolated modes by POD projection (Eq. 1). The spatial
range is then reduced to $Y_{FAST} = \pm 0.56\ D$ and $Z_{FAST} = [0, 1.38D]$ in a region close to the disk position and down to
the wall. Interpolation is also required to have a square grid and an equal number of points ($N_{p,y} = N_{p,z} = 31$). Finally, the
velocity fields are scaled to set the hub velocity $U_{hub,P} = 10$ m/s. Even if these operations are significant, features of the flow
are conserved, especially the reconstructed spatio-temporal dynamics of the flow obtained previously. All extrapolation and
interpolation operations are performed using bivariate B-spline functions (Dierckx, 1981).

As a reference, generic turbulent velocity fields are also generated using TurbSim (Kelley and Jonkman, 2007), the turbulence
generation tool provided with FAST. They correspond to velocity fields with prescribed boundary conditions and turbulence
intensity, but without any coherence of their dynamics. For the boundary layer, the power law exponent is $\alpha = 0.15$, the surface
roughness length $z_r = 0.01$ m. Four turbulence intensities profiles are chosen for these fields: for the first three datasets, the
turbulence intensities are set at the hub to 5 %, 7 % and 10 %. The last dataset follows the reference Normal Turbulence Model
(NTM) in IEC 61400-1 requirements (International Electrotechnical Commission, 2006). Class C is chosen from this model,
corresponding to the minimal turbulence class and a turbulence intensity of 12 % at the hub. The other parameters are the same
as the fields from experiments ($U_{hub,P} = 10$ m/s, $N_{p,y} = N_{p,z} = 31$).

Simulations are performed using FAST as implemented in the software Qblade (v0.963), developed by TU Berlin (Marten
et al., 2015). The tip-speed ratio (TSR) is fixed at 6.6, under the optimal value of 8 for this wind-turbine. The full-scale sampling
frequency for the simulations and the aerodynamical model is $F_{s,FAST} = 100$ Hz. The simulation time is $T_{s,FAST} = 6400$
s, larger than the requirements of 10min, to ensure statistical convergence. Global and local variables, such as thrust, torque
or strain gauges on the blades can be obtained. Only the power is presented here, the detailed analysis of the wind turbine
performance is left for future work.

275 **6.2 Results**

(a) **(b)**
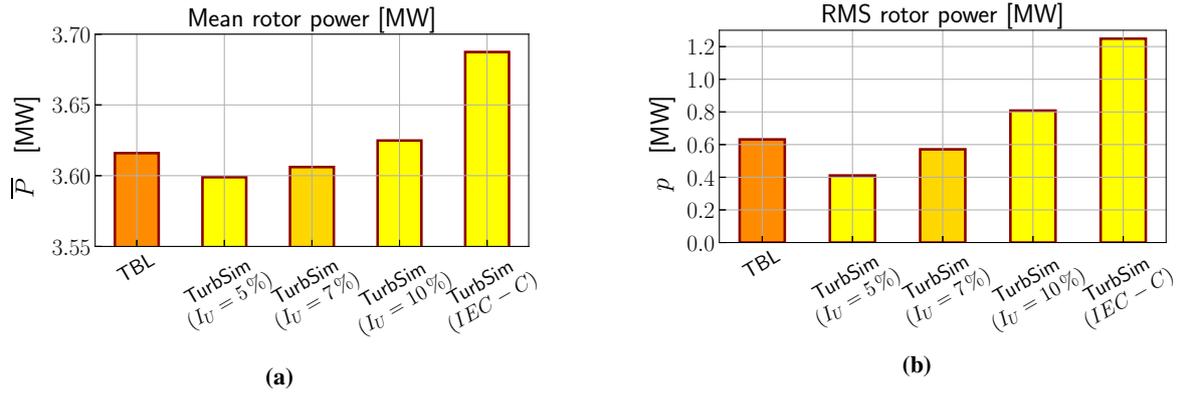
Figure 9. Comparison of the (a) mean and (b) RMS powers simulated with our experimental turbulent boundary layer (TBL) and the windfield datasets obtained with TurbSim, with four turbulence levels: $I_U = 5\%, 7\%, 10\%$ and reference Normal Turbulence Model in IEC 61400-1 requirements (class C).
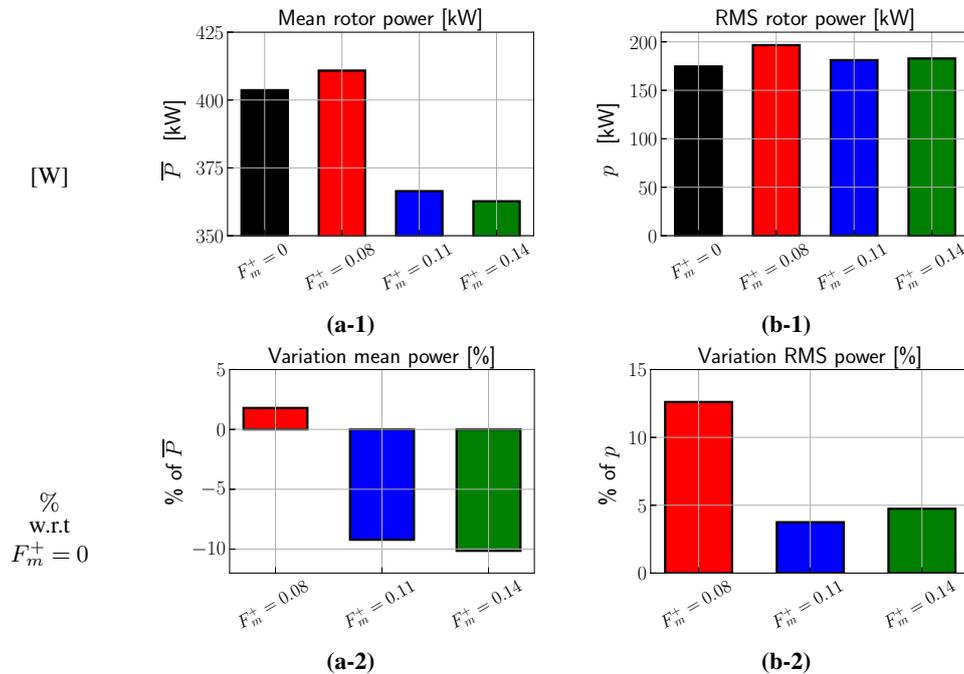
Figure 10. Effect of the wave-induced surge-motion on the powers obtained using Qblade / FAST simulations. (1) raw power; (2) variation in percent compared to the power without surge-motion. (a) mean rotor power for a second FOWT depending of the surge-motion frequency; (b) same but with RMS rotor power.

In order to demonstrate the benefit from using the proposed method, output rotor power obtained with the FAST simulations for different inlet flow configurations are presented in the current section. To ascertain the performances of the present approach against more standard techniques, output power of a single FOWT immersed in an atmospheric boundary layer are first presented in Fig. 9 and compared to simulations performed using the TurbSim turbulent inflow generator available in FAST.

280   The RMS velocity for the reconstructed TBL is around 7 % at the hub, as presented in Fig. 7. The mean power matches well for simulations with inputs using our experimental fields and TurbSim (Fig. 9 (a)). A difference up to 0.3% is observed between these mean powers with comparable RMS velocity, in particular with $I_U = 7$ %. The RMS power obtained with experimental fields also matches with the simulations with TurbSim datasets with similar turbulence levels. It should be noticed that the produced power is lower than 5MW due to the choice of the TSR.

285   In a second step, the ability of the present method to account for flow configurations more complex than the ABL alone is demonstrated by conducting FAST calculations of the performance of a wind turbine located in the wake of a first FOWT itself subjected to a surge-motion. Results are shown in Fig. 10. For a fixed upstream FOWT ($F_m^+ = 0.0$), the power produced for the second turbine decreased by 87 % compared to the unperturbed turbine. This difference is consistent with the power loss found in previous studies for an array of two turbines (Ceccotti et al., 2016; Bartl et al., 2012). For the lowest frequency tested

290   ($F_m^+ = 0.08$), the mean power is similar to the fixed model (less than 2% of difference). For higher frequencies ($F_m^+ > 0.11$), the calculated power drops significantly, corresponding to a decrease of -9.4% and -10.3% for surge-motions frequencies of $F_m^+ = 0.11$ and 0.14 respectively. RMS rotor power is shown to be particularly significant with respect to the mean power, approximately 50% of $\overline{P}$ for all cases. An increase of the RMS power is shown for all surge motions compared to the fixed model. The threshold at $F_m^+ = 0.11$ observed for the mean power is also important for the fluctuating component: this increase

295   of the RMS power is about 12 % for the lowest frequency, and $4-5$ % for higher frequencies.
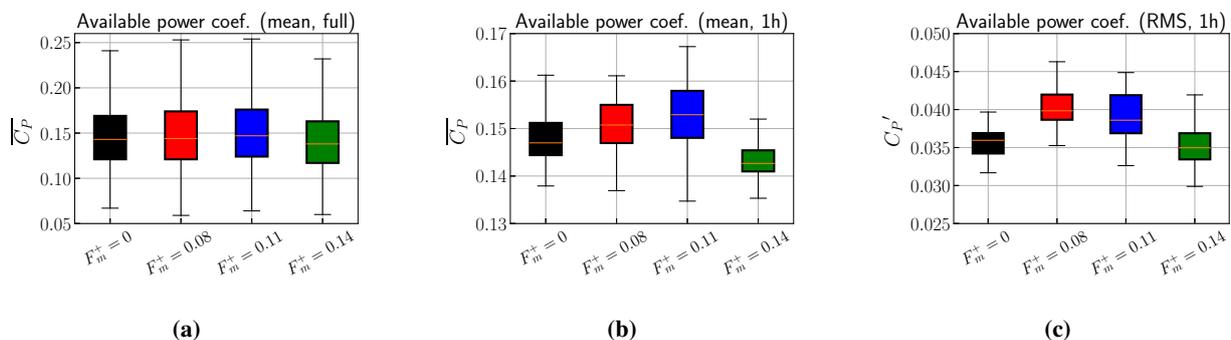
Figure 11. Statistics of the available normalized power computed directly from the inlet flow field. (a) Available power computed using the whole database; (b) and (c) mean and rms, respectively, of the available power computed over 1 hour periods. Box plots show the median (white), first and third quartiles (main box) and minimum and maximum values (wiskers).

The attention of the reader is drawn to the fact that in this section, the FAST calculations are performed over a single full-scale period of one hour, which is not long enough to obtain statistically significant results and draw any definite conclusion on the performance of a wind turbine subjected to the wake of FOWT and the impact of the surge motion of the latter. To

demonstrate this and the influence of the choice of the averaging period compared with the typical time scales of both the ABL
300 and the FOWT wake, statistics of the available power (AP) directly computed from the inflow velocity fields are shown in Fig.
11. Figure 11(a) shows the distribution of the instantaneous AP estimated over the entire inflow database. Besides the fact that
the range of variations is quite large, there is a clear trend in the median AP, with an increase with surge frequencies from 0
to $F_m^+ = 0.11$ and a drop for $F_m^+ = 0.14$. Distributions of the mean and rms AP estimated over 1-hour periods are shown in
Fig. 11(b) and (c), respectively. The range of variation of these short-period statistics can reach 25% of their median values.
305 It confirms the validity of the values estimated from the FAST calculations, which are within the range of variation of the
statistics. It also shows that the first identified trends due the influence of the surge frequency (Fig. 10) are not representative
and that a statistical analysis of the calculation output (which is beyond the scope of the present paper) is required to draw firm
conclusions.

7 Conclusions

310 A new method for generating inflow conditions for load simulations for wind turbines in complex configurations has been pre-
sented. It relies on interfacing the simulation code (FAST in the present case) with stereoscopic PIV wind-tunnel measurements
performed in a cross-section of the flow. This new approach has been tested in various flow configurations, including an ABL
only but also the wake of an upstream wind turbine (modeled by a porous disk in the wind tunnel) submitted to a surge-motion,
replicating the wave-induced movement a FOWT platform. The incoming motion was imposed with a fixed amplitude at four
315 different frequencies.

The boundary layer, turbulence levels and large coherent structures of the turbulent flow upstream the model are taken into
account in this study and are matching those of a realistic atmospheric flow. The wake was first characterized in a $y - z$ vertical
plane normal to the flow, at two streamwise positions via PIV and time-resolved hot-wire anemometry. By combining the two
types of measurements, velocity fields were reconstructed at higher sampling frequency using multi time-delay POD-LSE.
320 The temporal POD modes showed that the horizontal meandering and the vertical downwash are part of the main dynamics of
the wake, and therefore included in the data. The reconstructed velocities were subsequently implemented in FAST as inflow
conditions to estimate the performance (using FAST) of a full-scale 5MW wind turbine immersed in the wake of an upstream
wind turbine subjected to a surge motion. High frequencies of the upstream wind turbine lead to a significant reduction of the
power produced by the downstream turbine, up to 10.3 % for the highest frequency when compared to the case of an upstream
325 fixed wind turbine.

Coupling experimental data from wind tunnel and numerical simulations for the full-scale turbine constitutes the originality
of the approach presented here. The flow conditions (in particular the boundary layer and turbulence level) and the experimental
parameters (in particular the reconstructing sampling frequency) were chosen to match the requirements for FAST simulations.
Extrapolations used to adapt the velocity fields as FAST inputs do not alter the mean and unsteady dynamics of the flow.
330 As the spatial modes are unchanged (appendix A) and the physical differences are mainly contained in the temporal modes,
representative velocity fields can be easily generated using a reduced set of parameters. From a low-order modeling strategy, it

means that a unique set of spatial modes could be used, combined with artificial temporal modes having the proper dynamics in order to generate flow fields corresponding to generic floating wind turbines. It could allows for example real-time estimation of the wind turbine performances based on limited measurements on the full-scale prototype and *a priori* information from 335 wind tunnel data.

Appendix A: Details on the spatial POD modes
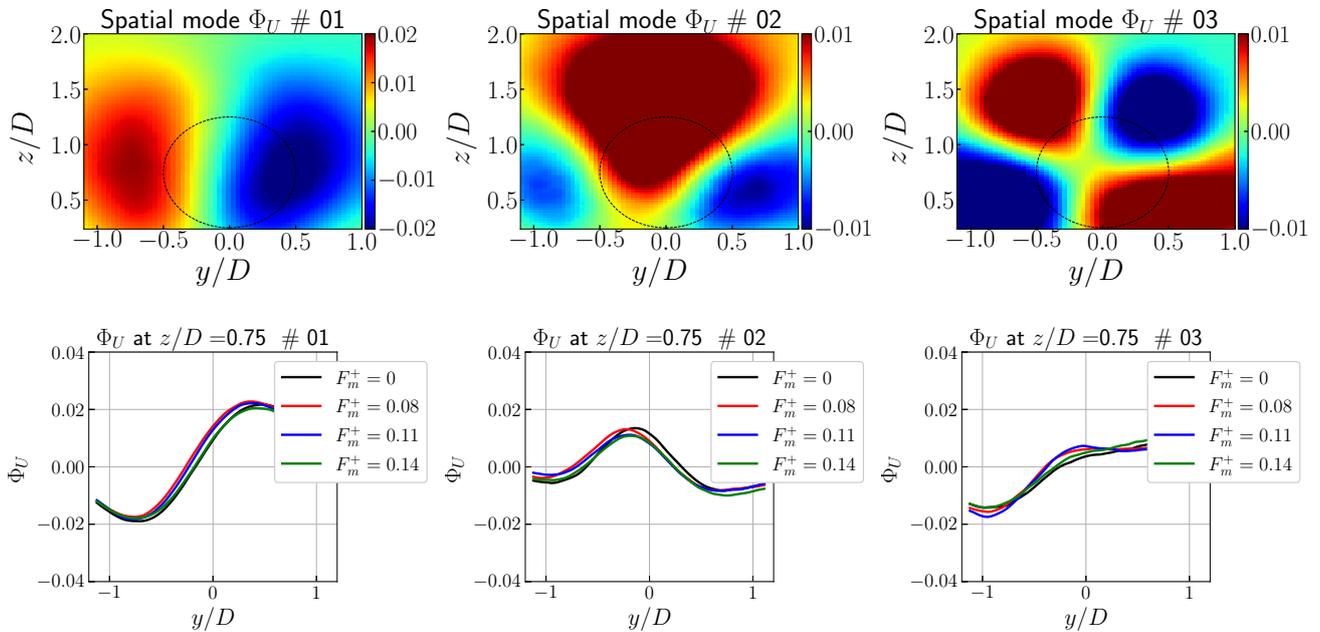
Figure A1. (a) Maps of spatial modes Φ_U for $x/D = 8.1$ for modes $i = 0$ to 2 and (b) profiles along the spanwise y direction at the hub height $z/D = 0.74$ with the effect of the surge-motion. (Raibaudo et al., 2022).

Spatial POD modes obtained from the database are presented. In particular, maps of the spatial modes of the streamwise velocity component Φ_U for $x/D = 8.1$ and profiles along the spanwise y direction and for two streamwise positions are presented in Fig. A1. Profiles are considered at the hub height ($z/D = 0.74$) and for different frequencies of surge-motion. 340 Modes signs are adapted for a better comparison. A more complete analysis of the POD modes for the floating wind turbine can be found in Raibaudo et al. (2022). As detailed in this previous work, no significant impact of the surge-motion is observed on the spatial modes of the streamwise velocity. Not shown here, the same is observed for the other velocity components spatial modes, Φ_v and Φ_w.

Author contributions. L.P. conceived of the presented idea, L.P. conceived and designed the experiments, C.R. and L.P. carried out the
345 experiments and collected the data, C.R. and JC.G. designed and analysed the FAST simulations, C.R. wrote the basic version of the paper,
C.R. and L.P. wrote the final version of the manuscript, L.P. supervised the project and got the funding. All authors provided critical feedback
and helped shape the research, analysis and manuscript.

Competing interests. The authors declare that they have no known competing interests or personal relationships that could have appeared to
influence the work reported in this paper.

350 *Acknowledgements.* The authors acknowledge the financial support of WEAMEC, the West Atlantic Marine Energy Community, under the
grant N° 2020 WIND2SIM. The authors are indebted to T. Piquet, research engineer at LHEEA, for his help during the experiments.

References

Aubrun, S., Loyer, S., Hancock, P. E., and Hayden, P.: Wind turbine wake properties: Comparison between a non-rotating simplified wind turbine model and a rotating model, Journal of Wind Engineering and Industrial Aerodynamics, 120, 1–8, https://doi.org/10.1016/j.jweia.2013.06.007, 2013.

Bartl, J., Pierella, F., and Sætran, L.: Wake measurements behind an array of two model wind turbines, Energy Procedia, 24, 305–312, https://doi.org/10.1016/j.egypro.2012.06.113, 2012.

Bastankhah, M. and Porté-Agel, F.: A new analytical model for wind-turbine wakes, Renewable Energy, 70, 116–123, https://doi.org/10.1016/j.renene.2014.01.002, 2014.

Bastine, D., Witha, B., Wächter, M., and Peinke, J.: POD analysis of a wind turbine wake in a turbulent atmospheric boundary layer, Journal of Physics: Conference Series, 524, https://doi.org/10.1088/1742-6596/524/1/012153, 2014.

Bastine, D., Witha, B., Wächter, M., and Peinke, J.: Towards a simplified dynamic wake model using POD analysis, Energies, 8, 895–920, https://doi.org/10.3390/en8020895, 2015.

Bastine, D., Vollmer, L., Wächter, M., and Peinke, J.: Stochastic wake modelling based on POD analysis, Energies, 11, 1–29, https://doi.org/10.3390/en11030612, 2018.

Belvasi, N., Conan, B., Schliffke, B., Perret, L., Desmond, C., Murphy, J., and Aubrun, S.: Far-Wake Meandering of a Wind Turbine Model with Imposed Motions: An Experimental S-PIV Analysis, Energies, 15, 1–17, https://doi.org/10.3390/en15207757, 2022.

Betz: Das maximum der theoretisch moglichen Auswendung des Windes durch Windmotoren, 1920.

Blackman, K. and Perret, L.: Non-linear interactions in a boundary layer developing over an array of cubes using stochastic estimation, Physics of Fluids, 28, https://doi.org/10.1063/1.4962938, 2016.

Bonnet, J. P., Cole, D. R., Delville, J., Glauser, M. N., and Ukeiley, L. S.: Stochastic estimation and proper orthogonal decomposition: Complementary techniques for identifying structure, Experiments in Fluids, 17, 307–314, https://doi.org/10.1007/BF01874409, 1994.

Camp, E. H. and Cal, R. B.: Mean kinetic energy transport and event classification in a model wind turbine array versus an array of porous disks: Energy budget and octant analysis, Physical Review Fluids, 1, https://doi.org/10.1103/PhysRevFluids.1.044404, 2016.

Canet, H., Bortolotti, P., and Bottasso, C. L.: On the scaling of wind turbine rotors, Wind Energy Science, 6, 601–626, https://doi.org/10.5194/wes-6-601-2021, 2021.

Ceccotti, C., Spiga, A., Bartl, J., and Sætran, L.: Effect of Upstream Turbine Tip Speed Variations on Downstream Turbine Performance, Energy Procedia, 94, 478–486, https://doi.org/10.1016/j.egypro.2016.09.218, 2016.

Chamorro, L. P. and Porté-Agel, F.: A wind-tunnel investigation of wind-turbine wakes: Boundary-Layer turbulence effects, Boundary-Layer Meteorology, 132, 129–149, https://doi.org/10.1007/s10546-009-9380-8, 2009.

Corniglion, R., Harris, J., Peyrard, C., and Capaldo, M.: Comparison of the free vortex wake and actuator line methods to study the loads of a wind turbine in imposed surge motion, Journal of Physics: Conference Series, 1618, https://doi.org/10.1088/1742-6596/1618/5/052045, 2020.

De Cillis, G., Cherubini, S., Semeraro, O., Leonardi, S., and De Palma, P.: POD-based analysis of a wind turbine wake under the influence of tower and nacelle, Wind Energy, 24, 609–633, https://doi.org/10.1002/we.2592, 2021.

Dekou, R., Foucaut, J. M., and Stanislas, M.: Large scale organization of a near wall turbulent boundary layer, in: 9th International Symposium on Turbulence and Shear Flow Phenomena, TSFP 2015, vol. 3, 2015.

Dierckx, P.: An algorithm for surface-fitting with spline functions, IMA Journal of Numerical Analysis, 1, 267–283, https://doi.org/10.1093/imanum/1.3.267, 1981.

390 Durgesh, V. and Naughton, J. W.: Multi-time-delay LSE-POD complementary approach applied to unsteady high-Reynolds-number near wake flow, Experiments in Fluids, 49, 571–583, https://doi.org/10.1007/s00348-010-0821-4, 2010.

Fontanella, A., Zasso, A., and Belloli, M.: Wind tunnel investigation of the wake-flow response for a floating turbine subjected to surge motion, Journal of Physics: Conference Series, 2265, https://doi.org/10.1088/1742-6596/2265/4/042023, 2022.

Foti, D., Yang, X., and Sotiropoulos, F.: Similarity of wake meandering for different wind turbine designs for different scales, Journal of
395 Fluid Mechanics, 842, 5–25, https://doi.org/10.1017/jfm.2018.9, 2018.

Foti, D., Yang, X., Shen, L., and Sotiropoulos, F.: Effect of wind turbine nacelle on turbine wake dynamics in large wind farms, Journal of Fluid Mechanics, 869, 1–26, https://doi.org/10.1017/jfm.2019.206, 2019.

Frandsen, S., Barthelmie, R., Pryor, S., Rathmann, O., Larsen, S., Højstrup, J., and Thøgersen, M.: Analytical modelling of wind speed deficit in large offshore wind farms, Wind Energy, 9, 39–53, https://doi.org/10.1002/we.189, 2006.

400 Fu, S., Jin, Y., Zheng, Y., and Chamorro, L. P.: Wake and power fluctuations of a model wind turbine subjected to pitch and roll oscillations, Applied Energy, 253, 113 605, https://doi.org/10.1016/j.apenergy.2019.113605, 2019.

Hamilton, N., Viggiano, B., Calaf, M., Tutkun, M., and Cal, R. B.: A generalized framework for reduced-order modeling of a wind turbine wake, Wind Energy, 21, 373–390, https://doi.org/10.1002/we.2167, 2018.

Hodgkin, A., Deskos, G., and Laizet, S.: On the interaction of a wind turbine wake with a conventionally neutral atmospheric boundary layer,
405 International Journal of Heat and Fluid Flow, 102, 109 165, https://doi.org/10.1016/j.ijheatfluidflow.2023.109165, 2023.

Huang, Y., Wan, D., and Hu, C.: Numerical Study of Wake Interactions between Two Floating Offshore Wind Turbines, Proceedings of the International Offshore and Polar Engineering Conference, 2018-June, 541–548, 2018.

Hultmark, M. and Smits, A. J.: Temperature corrections for constant temperature and constant current hot-wire anemometers, Measurement Science and Technology, 21, https://doi.org/10.1088/0957-0233/21/10/105404, 2010.

410 International Electrotechnical Commission: Wind turbines - Part 1: Design requirements, 2006.

Jensen, N. O.: A note on wind generator interaction, Risø-M-2411 Risø National Laboratory Roskilde, pp. 1–16, http://www.risoe.dk/rispubl/VEA/veapdf/ris-m-2411.pdf, 1983.

Jonkman, J., Butterfield, S., Musial, W., and Scott, G.: Definition of a 5-MW reference wind turbine for offshore system development, Tech. Rep. February, National Renewable Energy Lab.(NREL), Golden, CO (United States), http://tethys-development.pnnl.gov/sites/default/
415 files/publications/Jonkman_et_al_2009.pdf, 2009.

Joukowsky, N.: Windmill of the NEJ type, Transactions of the Central Institute for Aero-hydrodynamics of Moscow, 1, 57, 1920.

Kaldellis, J. K., Triantafyllou, P., and Stinis, P.: Critical evaluation of Wind Turbines' analytical wake models, Renewable and Sustainable Energy Reviews, 144, 110 991, https://doi.org/10.1016/j.rser.2021.110991, 2021.

Kelley, N. D. and Jonkman, B. J.: Overview of the TurbSim stochastic inflow turbulence simulator: Version 1.21 (revised february 1,
420 2001) (No. NREL/TP-500-41137)., Tech. Rep. April, National Renewable Energy Lab.(NREL), Golden, CO (United States), papers2://publication/uuid/84B33CE0-C9E4-4106-8CFC-7678530808B4, 2007.

Khosravi, M., Sarkar, P., and Hu, H.: An experimental investigation on the performance and the wake characteristics of a wind turbine subjected to surge motion, 33rd Wind Energy Symposium, pp. 1–11, https://doi.org/10.2514/6.2015-1207, 2015.

Mann, J.: Wind field simulation, Probabilistic Engineering Mechanics, 13, 269–282, https://doi.org/10.1016/s0266-8920(97)00036-2, 1998.

425   Marten, D., Lennie, M., Pechlivanoglou, G., Nayeri, C. N., and Paschereit, C. O.: Implementation, optimization and validation of a non-linear lifting line free vortex wake module within the wind turbine simulation code qblade, Proceedings of the ASME Turbo Expo, 9, https://doi.org/10.1115/GT2015-43265, 2015.

Messmer, T., Brigden, C., Peinke, J., and Hölling, M.: A six degree-of-freedom set-up for wind tunnel testing of floating wind turbines, Journal of Physics: Conference Series, 2265, https://doi.org/10.1088/1742-6596/2265/4/042015, 2022.

430   Nybø, A., Nielsen, F. G., Reuder, J., Churchfield, M. J., and Godvik, M.: Evaluation of different wind fields for the investigation of the dynamic response of offshore wind turbines, Wind Energy, 23, 1810–1830, https://doi.org/10.1002/we.2518, 2020.

Perret, L., Delville, J., Manceau, R., and Bonnet, J.-P.: Generation of turbulent inflow conditions for large eddy simulation from stereoscopic PIV measurements, International Journal of Heat and Fluid Flow, 27, 576–584, https://doi.org/10.1016/j.ijheatfluidflow.2006.02.005, 2006.

435   Perret, L., Delville, J., Manceau, R., and Bonnet, J. P.: Turbulent inflow conditions for large-eddy simulation based on low-order empirical model, Physics of Fluids, 20, https://doi.org/10.1063/1.2957019, 2008.

Podvin, B., Nguimatsia, S., Foucaut, J. M., Cuvier, C., and Fraigneau, Y.: On combining linear stochastic estimation and proper orthogonal decomposition for flow reconstruction, Experiments in Fluids, 59, 1–12, https://doi.org/10.1007/s00348-018-2513-4, 2018.

Porté-Agel, F., Bastankhah, M., and Shamsoddin, S.: Wind-Turbine and Wind-Farm Flows: A Review, vol. 174, Springer Netherlands,
440   https://doi.org/10.1007/s10546-019-00473-0, 2020.

Raibaudo, C. and Perret, L.: Low-Order Representation of the Wake Dynamics of Offshore Floating Wind Turbines, 12th International Symposium on Turbulence and Shear Flow Phenomena, TSFP 2022, pp. 1–6, 2022.

Raibaudo, C., Piquet, T., Schliffke, B., Conan, B., and Perret, L.: POD analysis of the wake dynamics of an offshore floating wind turbine model, Journal of Physics: Conference Series, 2022.

445   Rockel, S., Camp, E., Schmidt, J., Peinke, J., Cal, R. B., and Hölling, M.: Experimental study on influence of pitch motion on the wake of a floating wind turbine model, vol. 7, https://doi.org/10.3390/en7041954, 2014.

Rousset, J.-M., Mouslim, H., Le Bihan, G., and Babarit, A.: Le projet SEM-REV : un site d'expérimentation en mer pour la recherche et l'industrie, pp. 813–822, Centre Francais du Littoral, https://doi.org/10.5150/jngcgc.2010.090-r, 2010.

Saranyasoontorn, K. and Manuel, L.: Low-dimensional representations of inflow turbulence and wind turbine response using Proper Orthog-
450   onal Decomposition, Journal of Solar Energy Engineering, Transactions of the ASME, 127, 553–562, https://doi.org/10.1115/1.2037108, 2005.

Schliffke, B.: Experimental characterisation of the far wake of a modelled floating wind turbine as a function of incoming swell, Ph.D. thesis, École Centrale de Nantes, 2022.

Schliffke, B., Aubrun, S., and Conan, B.: Wind Tunnel Study of a "floating" Wind Turbine's Wake in an Atmospheric Boundary Layer with
455   Imposed Characteristic Surge Motion, Journal of Physics: Conference Series, 1618, https://doi.org/10.1088/1742-6596/1618/6/062015, 2020.

Schmidt, J. and Stoevesandt, B.: The impact of wake models on wind farm layout optimization, Journal of Physics: Conference Series, 625, https://doi.org/10.1088/1742-6596/625/1/012040, 2015.

Sirovich, L.: Turbulence and the dynamics of coherent structures. Part 2: Symmetries and transformations, Quarterly of Applied Mathematics,
460   15, 573–582, 1987.

VDI: Environmental meteorology - Turbulence parameters for dispersion models supported by measurement data, Tech. rep., Verein Deutscher Ingenieure, 2017.